Analytical Biochemistry 647 (2022) 114606

Contents lists available at ScienceDirect

Analytical Biochemistry

journal homepage: www.elsevier.com/locate/yabio

PET CMR_{glc} mapping and ^{1}H-MRS show altered glucose uptake and neurometabolic profiles in BDL rats

Jessie Mosso [a,b,c], Ting Yin [a,b], Carole Poitry-Yamate [a], Dunja Simicic [a,b,c], Mario Lepore [a,b], Valérie A. McLin [d], Olivier Braissant [e], Cristina Cudalbu [a,b], Bernard Lanz [a,b,c,*]

[a] CIBM Center for Biomedical Imaging, Switzerland
[b] Animal Imaging and Technology (AIT), EPFL, Lausanne, Switzerland
[c] Laboratory for Functional and Metabolic Imaging (LIFMET), EPFL, Lausanne, Switzerland
[d] Swiss Pediatric Liver Center, Department of Pediatrics, Gynecology and Obstetrics, University Hospitals Geneva, And University of Geneva, Geneva, Switzerland
[e] Service of Clinical Chemistry, Lausanne University Hospital and University of Lausanne, Lausanne, Switzerland

ARTICLE INFO

Keywords:
^{1}H MRS
^{18}F-FDG PET
Cerebral metabolic rate of glucose
Rat brain
Bile duct ligation
Type C hepatic encephalopathy

ABSTRACT

Type C hepatic encephalopathy (HE) is a complex neuropsychiatric disorder occurring as a consequence of chronic liver disease. Alterations in energy metabolism have been suggested in type C HE, but *in vivo* studies on this matter remain sparse and have reported conflicting results. Here, we propose a novel preclinical ^{18}F-FDG PET methodology to compute quantitative 3D maps of the regional cerebral metabolic rate of glucose (CMR_{glc}) from a labelling steady-state PET image of the brain and an image-derived input function. This quantitative approach shows its strength when comparing groups of animals with divergent physiology, such as HE animals. PET CMR_{glc} maps were registered to an atlas and the mean CMR_{glc} from the hippocampus and the cerebellum were associated to the corresponding localized ^{1}H MR spectroscopy acquisitions. This study provides for the first time local and quantitative information on both brain glucose uptake and neurometabolic profile alterations in a rat model of type C HE. A 2-fold lower brain glucose uptake, concomitant with an increase in brain glutamine and a decrease in the main osmolytes, was observed in the hippocampus and in the cerebellum. These novel findings are an important step towards new insights into energy metabolism in the pathophysiology of HE.

1. Introduction

Type C hepatic encephalopathy (type C HE) is a severe neuropsychiatric disorder occurring as a consequence of chronic liver disease, for which the prognosis is poor in the absence of liver transplantation [1]. In type C HE, cirrhosis with systemic shunting not only blocks blood flow; it hinders the liver's ability to filter and detoxify natural toxins, like ammonium, out of the body, thus facilitating toxin build-up in systemic blood travelling to the brain, where it adversely affects brain function. The understanding of biochemical mechanisms underpinning neurological and cognitive dysfunctions is still incomplete. So far, ammonium (NH_4^+) accumulation and glutamine (Gln) metabolism have been considered to play a central role in the pathophysiology of type C HE. Due to improper toxin clearance by the diseased liver, NH_4^+ accumulates in the systemic circulation before reaching the brain. Elevation in brain ammonia concentration leads to an excessive synthesis of brain Gln by the glutamine synthetase enzyme (GS), predominantly located in the astrocytes [2]. An increased astrocytic Gln content triggers an osmotic regulation mechanism shown by decreased concentrations of myo-inositol (Ins), taurine (Tau), total choline (tCho) and total creatine (tCr) measured by *in vivo* ^{1}H magnetic resonance spectroscopy (MRS), and consequently low-grade brain edema [3–5]. Alterations in energy metabolism have also been investigated *in vivo* in type C HE, yet only small or undetectable changes have been reported [6]. In the adult bile duct ligated (BDL) rat model of type C HE [7], no changes in reliably-quantified brain metabolites involved in energy metabolism (i.e. lactate (Lac), gamma adenosine triphosphate (γ-ATP)) have been observed using *in vivo* proton or phosphorus magnetic resonance spectroscopy [5,8,9] (^{1}H or ^{31}P MRS). Using carbon (^{13}C) MRS after ^{13}C-labelled glucose (Glc) injection, a steady-state increased Lac pool has been detected in BDL rats with uniformly labelled Glc [10], but no changes in brain mitochondrial fluxes have been measured in the same animal model following [1,6–$^{13}C_2$] Glc injections [11]. In the wider

* Corresponding author. CIBM Center for Biomedical Imaging, École polytechnique fédérale de Lausanne (EPFL), CIBM-AIT, CH F1 (Bâtiment CH), Station 6, CH-1015 Lausanne, Switzerland.
E-mail address: bernard.lanz@epfl.ch (B. Lanz).

https://doi.org/10.1016/j.ab.2022.114606
Received 31 October 2021; Received in revised form 6 February 2022; Accepted 13 February 2022
Available online 1 March 2022

Abbreviations

ADP	adenosine diphosphate
AIF	arterial input function
Ala	alanine
Asc	ascorbate
Asp	aspartate
ATP	adenosine triphosphate
BBB	blood brain barrier
BDL	bile duct ligated
bHB	β-hydroxybutyrate
CMR_{glc}	cerebral metabolic rate of glucose
Cr	creatine
FDG	fluorodeoxyglucose
FDG6P	fluorodeoxyglucose-6-phosphate
FOV	field of view
G6P	glucose-6-phosphate
GABA	γ-aminobutyric acid
Glc	glucose
Gln	glutamine
Glu	glutamate
GPC	glycerophosphocholine
GS	glutamine synthetase enzyme
GSH	glutathione
HE	hepatic encephalopathy
Ins	myo-inositol
Lac	lactate
LC	lumped constant
MIP	maximum intensity projection
MLEM	maximum likelihood expectation maximization
NAA	N-acetylaspartate
NAAG	N-acetylaspartylglutamate
PCho	phosphocholine
PCr	phosphocreatine
PE	phosphoethanolamine
PET	positron emission tomography
ROI	region of interest
Scyllo	scyllo-inositol
SD	standard deviation
SUV	standardized uptake value
SyN	symmetric deformable registration
Tau	taurine
tCho	total choline
tCr	total creatine
TE_{eff}	effective echo time
tNAA	total N-acetylaspartate
TR	repetition time
VOI	volume of interest
γ-ATP	gamma adenosine triphosphate

scope of energy metabolism studies in other preclinical models of HE (i.e. chronic portacaval-shunted rats and urease-induced hyperammonemic rats), autoradiography studies have reported conflicting results [12,13]. In addition, studies in patients with HE using positron emission tomography (PET) studies have focused on cirrhotic patients with mild HE only, and have shown a decreased ^{18}F fluorodeoxyglucose (^{18}F-FDG) uptake in the cingulate gyrus [14,15] and a hypermetabolism in the hippocampus [16,17]. A clinical case study of a patient with decompensated liver cirrhosis also showed a hypometabolism of glucose in the cerebellum and cerebral cortices [18]. However, to the best of our knowledge, no ^{18}F-FDG PET studies on preclinical models of type C HE are available to date.

In vivo localized ^{1}H MRS allows the non-invasive measure of metabolites involved in a variety of brain functions, such as osmoregulation (Ins, tCr), neurotransmission (Gln, Glutamate (Glu), γ-aminobutyric acid (GABA)) or energy metabolism (Lac). In the context of HE, *in vivo* longitudinal localized ^{1}H MRS has been acknowledged as a predictive tool of the early stages of the disease [19,20]. Moreover, when *in vivo* localized ^{1}H MRS is performed at ultra-high field (≥ 7 Tesla), the separation between Gln and Glu spectral peaks is feasible, allowing to disentangle the behaviour of these two crucial metabolites in the development of HE [5,9].

While ^{1}H MRS provides a steady-state information on metabolic pools, ^{18}F-FDG PET provides kinetic information on local brain glucose uptake. ^{18}F-FDG, an analog of glucose labelled with the positron-emitting ^{18}F, is transported across the blood-brain barrier and converted to ^{18}F-FDG-6-phosphate (analog of glucose-6-phosphate (G6P)) and no further metabolized through the glycolysis [21]. Therefore, the FDG PET signal at labelling steady-state reflects the very first two steps of glycolysis: glucose transport through the blood brain barrier (BBB) and phosphorylation to G6P. The standardized uptake value (SUV) is routinely reported in PET studies, but it does not allow for a quantitative assessment of glucose cerebral metabolic rates, especially in pathological conditions with alterations of systemic metabolism. The derivation of the glucose cerebral metabolic rate (CMR_{glc}) from labelling steady-state images is, on the contrary, a quantitative method introduced by *Sokoloff* et al. [21] for 2-deoxy-D-[^{14}C] glucose autoradiography studies, which can be extended to *in vivo* ^{18}F-FDG PET data and provides both a local and quantitative rate of glucose utilization in the tissue in a non-invasive way. Yet, it requires the dynamic measurement of the blood FDG activity (the arterial input function (AIF)) from the time of the bolus injection up to the labelling steady-state measurement time frame [22]. The measurement of the arterial input function can be particularly challenging in rodents and is often the more invasive part of the FDG-PET study. Following a recent strategy proposed by *Lanz* et al. [23], the AIF can be measured prior to the brain acquisition from the PET image of the vena cava where the FDG bolus is observed. In doing so, difficulties linked to manual and multiple blood samplings can be circumvented. By combining this dynamic measurement of the AIF with a static PET measurement on the brain at labelling steady-state, the CMR_{glc} can be derived from the sole PET scan for each animal with minimal invasiveness.

In the present work, we study how HE affects the first metabolic step in brain energetics, i.e. glycolysis, in the uptake and metabolism of blood-derived glucose. To this end, and presented in full, a novel ^{18}FDG PET-based methodology was developed to quantitate regional CMR_{glc}, using the image-derived AIF. The proposed ^{18}F-FDG PET quantification method results in 3D spatial mapping of glucose uptake in μmol/g/min. In addition, we combined the CMR_{glc} maps with *in vivo* ^{1}H MRS at 9.4T in the hippocampus and cerebellum, using a PET-to-atlas registration via intermediate MRI anatomical image co-registration, and showed regional alterations of brain glucose uptake in the BDL rat model of type C HE concomitant with neurometabolic pool changes. We focused on the hippocampus and cerebellum, as they are key regions involved in HE [24,25]. Taken together, ^{1}H MRS and quantitative ^{18}F-FDG PET bring a new insight on brain energy metabolism in HE.

2. Material and methods

2.1. BDL rats

We used the BDL rat model for chronic liver disease leading to type C HE, recognized by the International Society for Hepatic Encephalopathy and Nitrogen Metabolism (ISHEN) [7]. Male adult Wistar rats (n = 18,

Charles River Laboratories, France) underwent BDL (n = 10, 175 ± 13 g at surgery) or SHAM surgery (n = 8, 174 ± 14 g at surgery). Plasma bilirubin (Reflotron Plus analyzer, Roche, Switzerland) and blood ammonia (Integra 400 Plus, Roche, Switzerland) from the sublingual vein were measured at week 6 post-surgery in BDL rats to follow the disease progression. Ammonia was also measured at week 0 (prior to surgery). For all experiments, rats were under isoflurane anaesthesia (1.5–2% in a mixture of 50%/50% air/O_2 for MRS and 1–2% in 100% O_2 for PET) with the breathing rate maintained between 60 and 80 resp/minute (SA Instruments, USA). Body temperature was kept between 37.5 °C and 38.5 °C using a water bath system. All experiments were approved by the Committee on Animal Experimentation for the Canton de Vaud, Switzerland (VD3022.1).

2.2. ^{1}H MRS

^{1}H MRS experiments were performed in an actively shielded 9.4 Tesla horizontal magnet (Magnex Scientific, UK), 31-cm inner diameter bore, with a Direct Drive console (Varian Inc., USA) and a home-made transmit/receive quadrature surface radio-frequency coil. Anatomical T2-weighted images were acquired in the axial plane to position the volumes of interest (VOIs) for ^{1}H MRS scans using a multislice turbo-spin-echo sequence (repetition time (TR)/effective echo time (TE_{eff}) = 4000/52 ms, echo train length = 8, field of view (FOV) = 23 × 23 mm^2, slice thickness = 1 mm, 15 slices, matrix size = 256 × 256, 1 average). The SPECIAL [26] sequence was used for localized spectroscopy with TE = 2.8 ms, TR = 4 s, 160 averages (10 blocks of 16 averages), a 5 kHz spectral width and 4096 spectral points. To validate the disease state of the animals, ^{1}H MRS acquisitions were performed on BDL rats before surgery (week 0) and at 6 weeks post-surgery on two brain regions, hippocampus (week 0: n = 4, week 6: n = 9) and cerebellum (week 0: n = 3, week 6: n = 4), with a voxel size of 2.8 × 2 × 2 mm^3 and 2.5 × 2.5 × 2.5 mm^3 (x,y,z on Fig. 3), respectively. VAPOR [27] scheme was used for water suppression and FASTMAP [28] for shimming (target water linewidth in the hippocampus: 9–10 Hz, in the cerebellum: 14–17 Hz). Frequency drift and phase corrections between blocks were applied prior to absolute quantification of metabolites with LCModel [29] (version 6.2). An *in vitro* acquired metabolite basis set and the spectrum of macromolecules measured *in vivo* [30,31] were used for LCModel quantification. The following 20 metabolites were included in the basis set: alanine (Ala), ascorbate (Asc), aspartate (Asp), β-hydroxybutyrate (bHB), glycerophosphocholine (GPC), phosphocholine (PCho), creatine (Cr), phosphocreatine (PCr), GABA, Glc, Gln, Glu, glutathione (GSH), Ins, Lac, N-acetylaspartate (NAA), N-acetylaspartylglutamate (NAAG), phosphoethanolamine (PE), scyllo-inositol (Scyllo), and Tau. The water signal from the same voxel was used as internal reference and the metabolite concentrations were derived from the ratio of peak areas, assuming that the water concentration in the voxel was 44.4 M. An exclusion criterion for individual metabolite concentrations based on relative Cramer Rao Lower Bounds (rejected if CRLB > 35%) was used. In addition, metabolites were not reported if more than 75% of quantified concentrations over the investigated group were rejected. Since ^{1}H MRS acquisitions were performed at week 0, each animal served as its own control for ^{1}H MRS results at week 6.

2.3. ^{18}F-FDG PET

PET acquisitions on BDL (n = 10) and SHAM (n = 8) rats at week 6 post-surgery were conducted on a small animal avalanche photodiode detector-based LabPET-4 scanner, with 250–650 keV energy window and 22.2 ns coincidence time window (Advanced Molecular Imaging, Canada). The acquisitions for each individual rat were performed and reconstructed in two steps:

Step (1). a 45-min dynamic acquisition on the thoracic region of the animal to extract the image-derived AIF from the vena cava, followed by,

Step (2). a static acquisition at labelling steady-state with the rat brain in the FOV of the PET scanner, to further calculate [21] CMR_{glc} maps of the brain.

For step (1), a 60 mm-diameter cylindrical field of view (FOV) in the coronal plane and 36.6 mm in the axial direction (31 slices of 1.18 mm thickness) was positioned on the thoracic region of the rat and a bolus of ^{18}F-FDG (67.6 ± 11.9 MBq) was injected in the tail vein, followed by a saline chase. Coincidence data were acquired in list mode to allow for a flexible reconstruction of time frames. Dynamic radioactivity density maps were quantified in Bq/ml using the LabPET-4 built-in calibration method and reconstructed using the iterative MLEM algorithm (5 iterations), with a time resolution enabling a good characterization of the bolus input function (24 × 5 s, 6 × 30 s, 5 × 120 s, 6 × 300 s) [23]. The inferior vena cava was then identified from the maximum intensity projection (MIP) images during the FDG bolus passage, using the PMOD software environment (PMOD Technologies Ltd.). The AIF was then extracted from the dynamic PET images from step (1) by averaging the activity in Bq/mL of 4 voxels over 4 successive axial slices (total volume: 4.7 mm^3) on the vena cava where the flow of ^{18}F-FDG was observed.

Following step (1), a 10 to 15 min-static acquisition on the brain was performed for step (2) (0.5 × 0.5 × 1.18 mm^3 standard voxel size, 60 mm-diameter coronal FOV, 31 axial slices of 1.18 mm thickness) and the quantified images in Bq/mL were reconstructed with a 15-iteration maximum likelihood expectation maximization (MLEM) algorithm [32].

During post processing, the AIF curve from step (1) was first corrected for radioactivity decay and blood versus plasma tracer content [33]. It was then extrapolated from the end of the dynamic acquisition up to the central time of the static acquisition used in step (2) based on a bi-exponential fit started at t = 2 min (i.e. in the decaying phase of the AIF following the chase). In the calculation of the CMR_{glc}, trapezoidal integration of the extrapolated AIF curve was used. Brain images were corrected for radioactivity decay from the start of the vena cava acquisition (step (1)).

Finally, 3D maps of CMR_{glc} were reconstructed following the 2-deoxy-D-[^{14}C]glucose quantification method of *Sokoloff* et al. [21]. In this method, the CMR_{glc} is obtained from a three-compartment model, represented in Fig. 1: a pool 1 of plasma Glc and ^{18}F-FDG, a pool 2 of intracellular Glc and ^{18}F-FDG, and a pool 3 of intracellular G6P and ^{18}F-FDG6P. The following 4 hypotheses were made. First, the static measurement is performed at a sufficiently late time point and in a homogeneous region such that the kinetic rates, the transport rates, the Glc plasma concentration, all intracellular concentrations and the CMR_{glc} rate are constant. In our extension of this method to 3D CMR_{glc} maps from static FDG-PET images, this assumption of homogeneous region applies to the reconstructed voxel. Second, the ^{18}F-FDG and ^{18}F-FDG6P concentrations are present in tracer amounts compared to their non-radioactive counterpart. Third, the hydrolysis of G6P to Glc and ^{18}F-FD6P to ^{18}F-FDG can be neglected compared to the reverse phosphorylation step. Forth, all brain regions receive a similar amount of tracer and Glc. From these hypotheses, the CMR_{glc} value was derived, describing the rate of G6P utilization in the tissue [21]:

$$CMR_{glc} = \frac{C_i^*(T) - k_1^* e^{-\left(k_2^*+k_3^*\right)T} \int_0^T C_p^* e^{+\left(k_2^*+k_3^*\right)t} dt}{LC \times \left[\int_0^T \frac{C_p^*(t)}{C_p} dt - e^{-\left(k_2^*+k_3^*\right)T} \int_0^T \frac{C_p^*(t)}{C_p} e^{+\left(k_2^*+k_3^*\right)t} dt\right]} \quad (1)$$

where C_i^* is the summed concentration of intracellular radioactive compounds (^{18}F-FDG6P and ^{18}F-FDG) i.e. the quantity measured at steady-state in a PET experiment, T the central time of the steady-state static acquisition after the bolus injection, k_1^* the kinetic rate of ^{18}F-FDG transport from pool 1 to pool 2 through the BBB, k_2^* the reverse ^{18}F-FDG transport rate from pool 2 to pool 1, k_3^* the ^{18}F-FDG

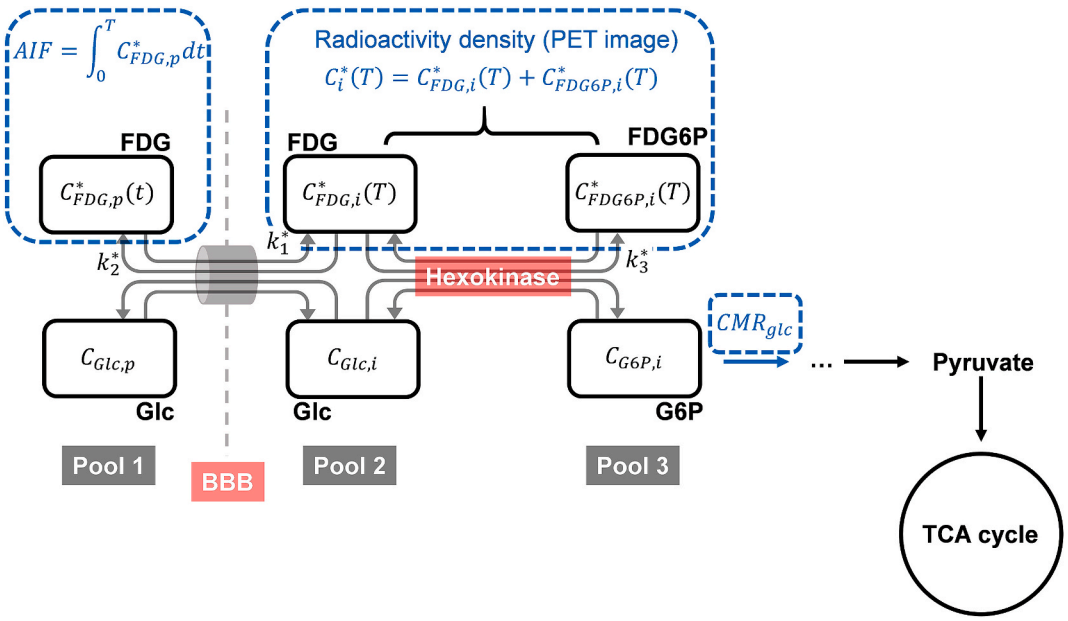

Fig. 1. Three-compartment model of glucose and FDG metabolism used to compute CMR_{glc} values: the kinetic constants, k, and the pool concentrations, C, are denoted with a * when related to the radiolabeled compounds. Subscripts *i* and *p* are intracellular and plasma, respectively. The PET measured or derived quantities are highlighted in blue.

phosphorylation rate into ^{18}F-FDG6P, C^*_p the time-dependent plasma ^{18}F-FDG concentration and C_p the constant plasma Glc concentration. It is assumed that the chemical reaction between FDG and FDG6P is at equilibrium and that partial volume effect (additional radioactivity from the blood vessels measured in the tissue) is negligible when T is large.

If T is large enough (experimentally, 45 min), equation (1) can be approximated by [21]:

$$CMR_{glc} = \frac{C^*_i(T) \times C_p}{LC \times \int_0^T C^*_p(t)dt} \quad (2)$$

where $\int_0^T C^*_p(t)dt$ is the integral of the AIF from step (1) of the *in vivo* acquisition and $C^*_i(T)$ the steady-state brain radioactivity density, as measured from the PET images from step (2). LC is the Lumped Constant, which accounts for the competition between Glc and ^{18}F-FDG at the transport and phosphorylation steps, as both substrates use the same BBB transporters [34] and are phosphorylated by hexokinase [35]. In our study, the Lumped Constant (LC) was set to 0.71, as done previously in rat brain studies [36]. Glycemia C_p was measured at the end of step (2) in the tail vein. Since $C^*_i(T)$ is measured for each image voxel from the steady-state acquisition over the brain (step (2)), the derivation of the CMR_{glc} results in a 3D metabolic CMR_{glc} map with the same nominal spatial resolution as the PET acquisition itself (i.e. 0.5 × 0.5 × 1.18 mm ^{3}), individually for each animal.

2.4. PET-atlas registration

Since PET images inherently suffer from low spatial resolution and poor anatomic contrast, direct PET to atlas registration is challenging. To circumvent this limitation, the MRI anatomical images of one rat were used as an intermediate registration step (see the procedure described in Fig. 2). The CMR_{glc} map from one animal with its corresponding MRI anatomical images were chosen as a reference pair. In step A, this reference CMR_{glc} map was registered to its corresponding MRI image using mutual-information-based rigid transformation [37], and in step B, to the Waxholm Space Atlas [38] using affine and nonlinear symmetric deformable registration (SyN) through the Advanced Normalization Tools [39]. In step C, all other individual CMR_{glc} maps were registered to the reference CMR_{glc} map by applying rigid and seven-degrees of freedom similarity transformation with normalized gradient field similarity measure in MeVisLab [40]. Following step C, atlas labels were resampled to each individual PET space to perform a region of interest (ROI)-based analysis, where CMR_{glc} maps were averaged over the hippocampus and the cerebellum regions, respectively.

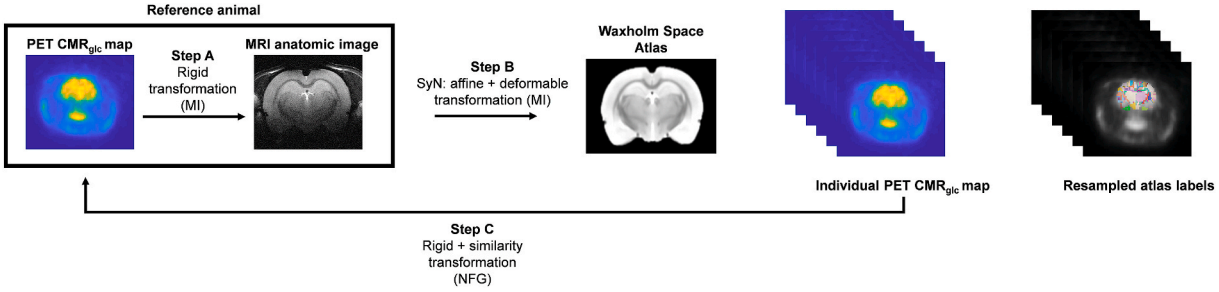

Fig. 2. PET to atlas registration: the CMR_{glc} map of a reference animal was first registered to its corresponding MRI anatomical images, and then to the Waxholm Space Atlas [38]. Other CMR_{glc} maps were then aligned with the reference one to obtain segmentations for the cerebellum and hippocampus. SyN: nonlinear symmetric deformable registration, MI: mutual information, NFG: normalized field gradient.

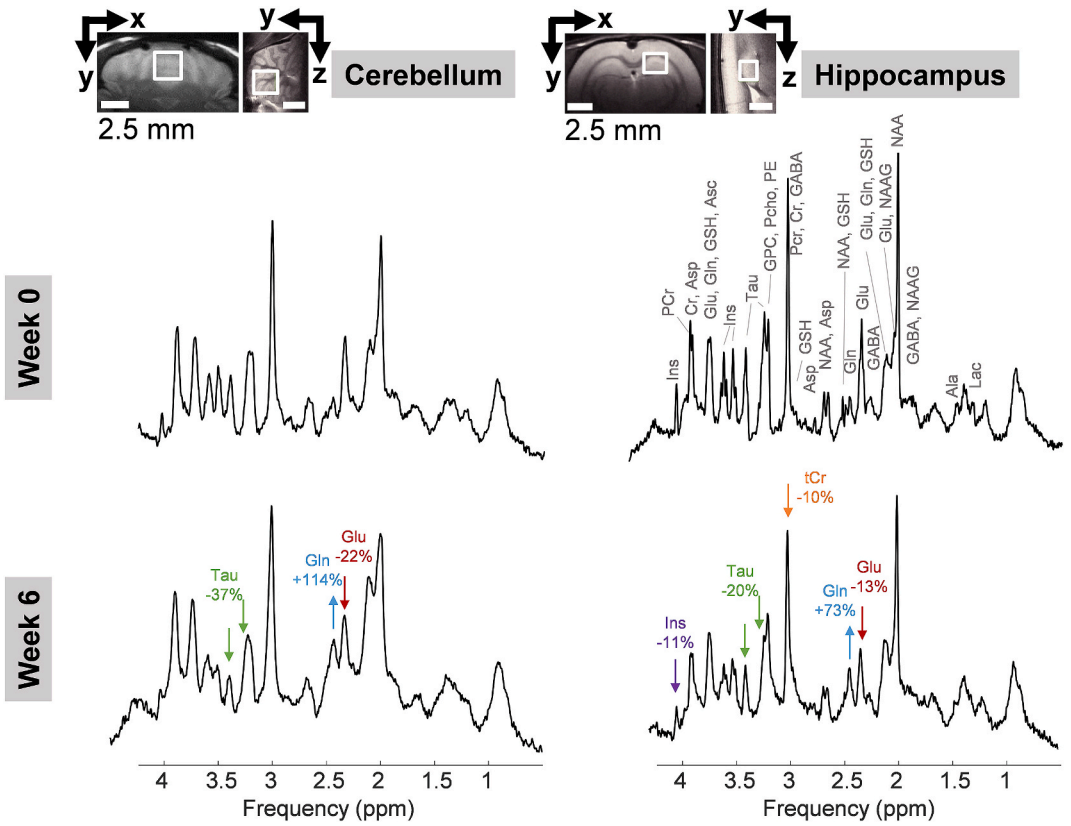

Fig. 3. ^{1}H MRS spectra acquired at 9.4 T in the hippocampus and cerebellum of BDL rats at week 0 and 6 post-surgery. Arrows show significant differences observed between week 0 and week 6 for each brain region, and point solely to non-overlapping (or least-overlapping) peaks for the displayed metabolites. The two voxels on anatomical T2-weighted images are shown at the top, where (x,y,z) are the MRI gradient directions.

2.5. Statistical analysis

All data are presented as the mean ± standard deviations (SD) and assumed to be Gaussian-distributed. Variance equality was tested prior to any statistical test using a Fisher test (F-test of equality of variances). For plasma bilirubin and blood ammonia measurements, an unpaired Student's *t*-test between week 0 and 6 blood or plasma concentrations was performed. For brain volumes, the mean of the total brain volume covered by all atlas labels derived from the PET to atlas registration was compared between SHAM and BDL rats using an unpaired Student's *t*-test.

For ^{1}H MRS, only Asc concentrations in the hippocampus featured non-equal variances between week 0 and week 6. All metabolite mean concentrations ± SD at week 0 and week 6 were therefore compared using an unpaired Student's *t*-test, except for Asc concentrations in the hippocampus which was compared with a Welch's *t*-test, accounting for unequal variances.

For all metabolites where both brain regions displayed significant changes between week 0 and 6 (Gln, Glu and Ins + Tau + tCr + tCho), the impact of the brain region on concentration changes over the weeks was tested through the interaction of the week factor and the brain region factor in a two-way ANOVA (Prism 5.03, Graphpad, La Jolla CA US).

For ^{18}F-FDG PET, CMR_{glc} variances between SHAM and BDL rats for each brain region were found equal, thus mean CMR_{glc} ± SD were compared using a Student's *t*-test. We also checked that the standard error on the mean CMR_{glc} over the region of interest was smaller than the SD in the mean CMR_{glc} between animals, retrospectively ensuring that using the SD was meaningful.

The following statistical significance values were used: *p < 0.05, **p < 0.01, ***p < 0.001, ****p < 0.0001.

3. Results

3.1. Biochemical measurements

Plasma bilirubin (<0.5 mg/dl at week 0 [5] to 8.07 ± 2.03 mg/dl at week 6, n = 1,****) and blood ammonia (89 ± 43 μM at week 0, n = 4 to 127 ± 25 μM at week 6, n = 4, not significant) increased in all BDL rats, confirming the induced chronic liver disease (supplementary material, Fig. S1).

3.2. ^{1}H MRS - impaired neurometabolic profiles in BDL rats

Representative spectra acquired in BDL rats at week 0 and 6 in both brain regions are shown in Fig. 3. In the hippocampus, the group analysis showed a strong increase of Gln between week 0 and 6 (+73%,***), and a decrease of Glu (−13%,**), Tau (−20%,**), Ins (−11%, *), total creatine (Creatine + Phosphocreatine, tCr) (−10%,****) and Asc (−17%,**). In the cerebellum, the group analysis showed an increase of Gln, which was even stronger than the one in the hippocampus (+114%,***, with a 1.6-fold significant difference in % change between the two brain regions,*), a decrease of Glu (−22%,**) and Tau (−37%,**), but no significant difference was observed for tCr, Ins and Asc. GABA also showed a significant decrease in the cerebellum (−43%,*). Additionally, the main metabolites playing a role in osmoregulation (tCr, tCho, Ins, Tau) were summed to evaluate the osmoregulatory response to the Gln-induced osmotic stress and a significant decrease was observed in the hippocampus (−13%,***) and in the cerebellum (−15%,*), as shown in Fig. 5C. All other individual metabolites that were reliably quantified (GSH, Lac, PE, total N-acetylaspartate (tNAA), and total choline (tCho)) showed no significant difference between week 0 and 6 in any of the two brain regions. Ala, Asp, Scyllo, bHB

and Glc were present in the basis set but were excluded from the analysis. The mean metabolite concentrations (referenced to water) at week 0 and 6, as well as the CRLB and the mean metabolite concentrations referenced to tCr are presented in tables S3 and S4 in Supplementary Materials.

3.3. ^{18}F-FDG - impaired glucose uptake in BDL rats

The image-derived AIF was reliably measured for each rat from the radiotracer bolus observed in the vena cava during the 45 min dynamic acquisition. Fig. 4A shows a representative AIF prior to correction for blood/plasma FDG content, as well as the chosen VOI over the vena cava based on the maximum intensity projection image. The higher temporal resolution at the beginning of the AIF acquisition allowed for accurate mathematical integration of the input function in the period when the bolus and the chase induced a fast variation of blood FDG activity. The CMR_{glc} derivation from the step (2) PET acquisition over the brain at steady-state enabled the reconstruction of high resolution 3D metabolic maps for individual animals with the same spatial resolution as the reconstructed PET images. A typically two-fold lower CMR_{glc} was observed in BDL versus SHAM rats on all axial slices (Fig. 4B shows an example of CMR_{glc} maps obtained on one BDL and one SHAM rat).

PET to atlas registration through MRI anatomic images enabled a ROI-specific measure of glucose uptake and a quantitative comparison between PET and ^{1}H MRS data in the hippocampus and the cerebellum. Fig. 5A shows the atlas labels for the two brain regions. A significant 2.66-fold and 2.53-fold smaller CMR_{glc} in BDL rats compared to SHAM rats (Fig. 5B) was measured respectively in the cerebellum (SHAM: 0.337 ± 0.064 μmol/g/min, BDL: 0.127 ± 0.052 μmol/g/min, ****) and in the hippocampus (SHAM: 0.348 ± 0.068 μmol/g/min, BDL: 0.138 ± 0.063 μmol/g/min, ****). The proposed co-registration provided quantitative metrics to the differences observed globally in the axial slices of the CMR_{glc} maps (Fig. 4B).

Fig. 5C summarizes the ^{1}H MRS results presented in Fig. 3, together with the colocalized PET results presented in Fig. 4, allowing to draw an overall picture of glucose uptake and neurometabolic profiles alterations happening in BDL rats at week 6 in both brain regions. The BDL rats showed a smaller CMR_{glc} (i.e. smaller glucose uptake) in both regions, an increase in glutamine (cerebellum: +114%, hippocampus: +73%), decrease in Glu (cerebellum: 22%, hippocampus: 13%) and main osmolytes (cerebellum: 15%, hippocampus: 13%), compared to control rats, together with a decrease in some low concentrated metabolites (Asc in the hippocampus (−17%), and in GABA in the cerebellum (−22%)). Additionally, Gln increase was significantly stronger in the cerebellum compared to the hippocampus (week 0–6% change), and Glu, Tau and CMR_{glc} show a stronger decrease (although not statistically significant) in the cerebellum.

4. Discussion

The present study proposes a new quantification method to extract quantitative information on the glucose metabolic rate from the raw PET image. This was made possible by using for the first time the combination of the image-derived AIF measurement [23] and the derivation of CMR_{glc} maps using the *Sokoloff* et al. approach [21], associated with the registration of PET images to a rat brain atlas through MRI T2-weighted anatomic acquisitions. This new approach rendered the 3D PET image fully quantitative and provided an easier experimental implementation with minimal invasiveness of the AIF acquisition as compared with the standard technique employing repeated manual blood samplings. Consequently, we also report here the first *in vivo* study in BDL rats using both ^{18}F-FDG PET and ^{1}H MRS to map brain glucose uptake concomitant with the measurement of brain metabolite alterations, bringing a new insight into brain energy metabolism in HE.

4.1. Consequences of ammonia load on neurometabolic profiles in BDL rats

The increase in Gln and decrease in osmolytes (Ins, Tau, tCr) observed in the present study are in agreement with a previously published study in the hippocampus of BDL rats [5]. Very interestingly, this important finding was observed here using even fewer animals. Ins, tCr and Tau have been suggested as regulators of cellular volume during induced swelling [41,42], here caused by the Gln load in the astrocytes, and where an efflux could help to restore the osmotic balance.

A primary explanation for decreased Glu in the two brain regions analyzed in this study arises from its excessive use, together with ammonia, for GS-mediated Gln production [5,43]. In addition, altered neurotransmission, both glutamatergic [44] and GABAergic [45,46], has also been proposed as a consequence of chronic hyperammonemia, which could reflect the decrease in Glu observed in both regions and the decrease of GABA in the cerebellum.

The benefit of the spectral separation of Gln/Glu with ^{1}H MRS spectroscopy at 9.4 T confirms its importance in the context of HE. Indeed, the combined reduction of Glu and increase in Gln concentrations could partially compensate each other when only measuring Glx, the sum of Glu and Gln, a common limitation in ^{1}H MRS at lower fields. In addition, the cerebellum appears more vulnerable to metabolic

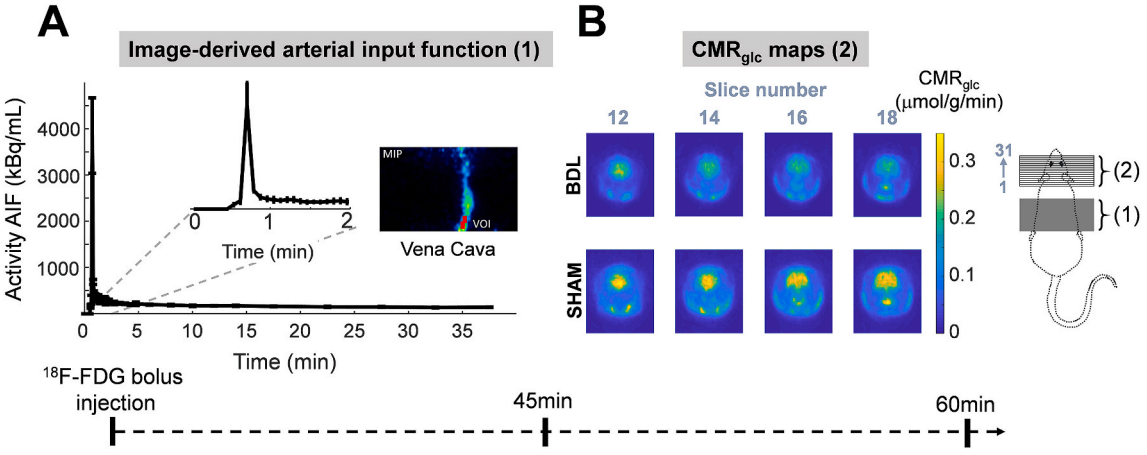

Fig. 4. ^{18}F-FDG PET arterial input function and CMR_{glc} maps acquired in BDL and SHAM rats. A. Representative arterial input function curve before correction for blood/plasma content [33], with corresponding VOI in the vena cava. B. Typical CMR_{glc} maps in a BDL and a SHAM rat for four central slices. The rightmost part of the figure shows the position of the PET scanner FOV for the two acquisitions and the slice order. The time repartition of the two acquisitions after injection of the radiotracer is shown at the bottom.

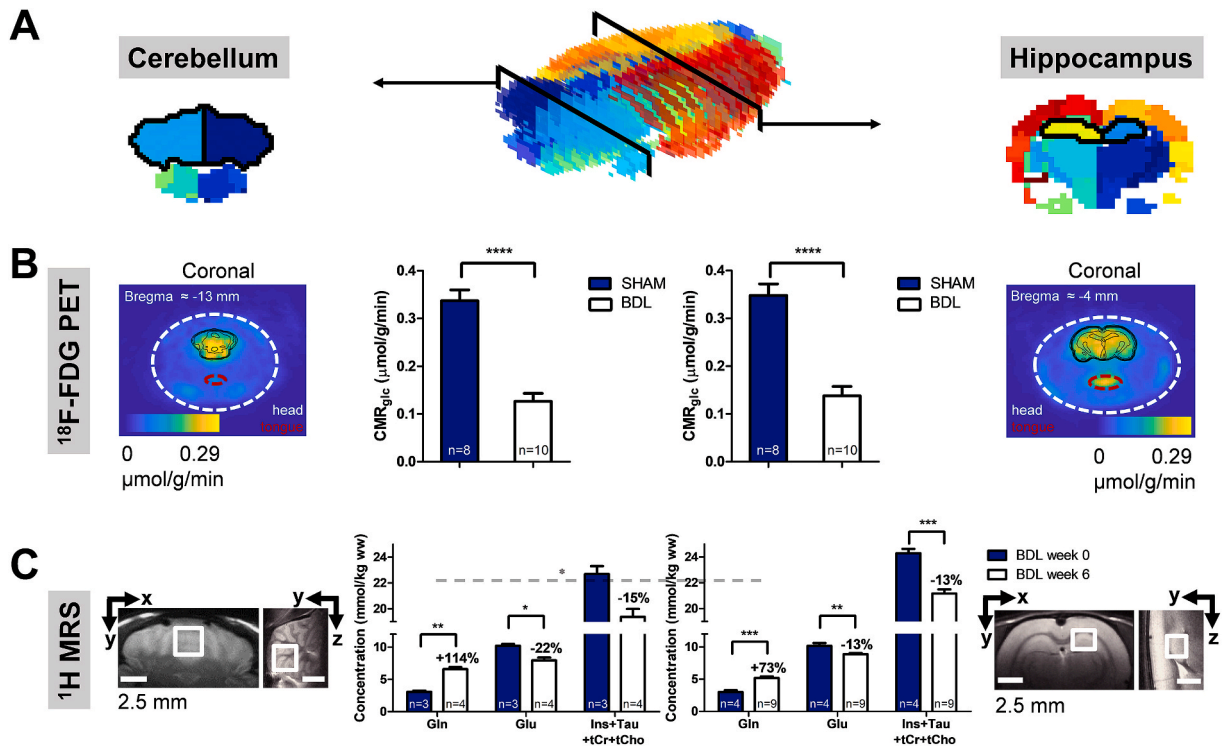

Fig. 5. Atlas-based co-localization of ^{1}H MRS and ^{18}F-FDG PET. A. Color-coded atlas regions, with the regions of interest (cerebellum and hippocampus) highlighted by solid lines. B. ^{18}F-FDG PET CMR_{glc} values averaged over the atlas labels of the cerebellum and hippocampus. C. ^{1}H MRS metabolite quantifications in a voxel localized in the cerebellum and in the hippocampus. Low concentrated metabolites (Asc, GABA) are not displayed. kg ww stands for kilograms wet weight. (For interpretation of the references to color in this figure legend, the reader is referred to the Web version of this article.)

changes compared to the hippocampus in BDL rats, confirming previously reported work in this rat model [47].

The Asc decrease in the hippocampus of BDL rats measured in this study is in line with another ^{1}H MRS study reported previously in BDL rats [5]. Of note, Asc absolute concentrations should be interpreted with care, as it is a low-concentrated and overlapping metabolite, but its relative decrease between week 0 and 6 is informative. Asc is playing an antioxidant role, therefore its decrease is usually linked to the oxidative stress occurring in the pathogenesis of HE [48] and is also in agreement with one of our previous studies where EPR was used as a complementary technique to validate the ^{1}H MRS changes [49].

4.2. Impaired energy metabolism in BDL rats

Our present findings suggest an altered energy metabolism in BDL rats measured with ^{18}F-FDG PET, in agreement with a Glc hypometabolism observed in a patient with decompensated cirrhosis using FDG PET [18]. In contrast, a previous longitudinal study using ^{1}H MRS and ^{31}P MRS on BDL rats has reported no change in the steady-state concentrations of energy metabolites (i.e. Adenosine triphosphate (ATP), tCr, Lac, while Glc was not reported after week 4) before week 8 post-surgery, with only Adenosine diphosphate (ADP) showing a significant decrease at week 8 post-BDL [8]. This discrepancy can be explained by the different nature of MRS and PET measurements and the complementary information that they provide. While ^{1}H MRS measures metabolic pool sizes and reflects the equilibrium changes of biochemical reactions, PET is a kinetic probe that informs on glucose metabolic fluxes. Additionally, it has been shown that brain tissue Glc measured by ^{1}H MRS tends to reflect the concentration of plasma Glc if the later varies sufficiently slowly [50,51], thus informing on Glc homeostasis rather than its metabolism. Glc pools are also challenging to measure using ^{1}H MRS because Glc is strongly overlapping with other metabolites on the upfield region of the spectra and with the water residual on the downfield region. Finally, ADP and ATP pools could remain constant if alternative substrates to glucose (such as Lac [10] or ketone bodies [52]) were to be used in the TCA cycle, but more exploratory work in BDL rats is required to test this hypothesis, as well as its link with a potential impairment of the Gln/Glu cycle [9].

4.3. CMR_{glc} versus standardized uptake value (SUV)

Previously published ^{18}F-FDG PET studies in HE [12–14] in patients and preclinical models show little or no impairment in glucose uptake, whereas we observed a strong difference between BDL and SHAM rats. In addition to the expected difference in HE type (chronic or acute, minimal or overt) and disease characteristics between human and animal studies, we believe that this discrepancy is mainly due to the method used to quantify ^{18}F-FDG PET data.

While most studies use the SUV (in g/ml, defined as the ratio between the quantified radioactivity density maps of the brain in Bq/ml and the fraction of the injected dose (Bq) divided by the weight of the animal (g)), the CMR_{glc} is rarely exploited. The SUV is widely used for its robustness and simplicity but is only a semi-quantitative approach, reflecting the normalized density of the tracer distribution in the brain. Its normalization is derived from a macroscopic information (fraction of the injected FDG dose over the weight of the animal) that may overlook subtle changes in the physiology of the animal.

To illustrate this point, the comparison between the CMR_{glc} and the SUV for both groups for the hippocampus and cerebellum is shown in Fig. 6A and B. Both CMR_{glc} and SUV calculation methods start with the same radioactivity density images acquired at FDG labelling steady-state. Fig. 6C shows the normalization terms involved in the CMR_{glc} formula (integral of the AIF and final blood glycemia – C_p) and in the SUV formula (injected dose of FDG and weight of the animal). No difference between BDL and SHAM rats in either of the two investigated brain regions can be detected with the SUV (Fig. 6A and B, hippocampus

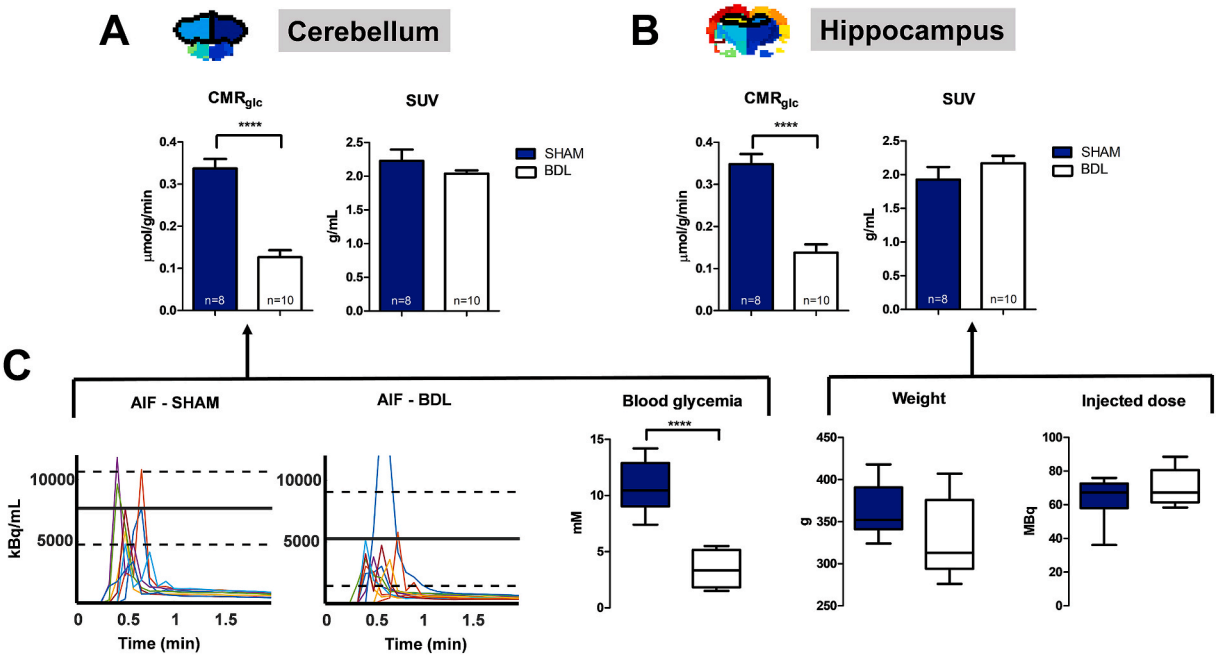

Fig. 6. Comparison between two different metrics for PET data, the fully-quantitative CMR_{glc} and the semi-quantitative SUV for the cerebellum (A) and the hippocampus (B) (color-coded atlas regions, with the regions of interest (cerebellum and hippocampus) highlighted by solid lines) and its respective normalization terms (C). Individual arterial input function curves from each animal are displayed in the left part of panel C, the full line being the mean of the maximum of the AIF and the dashed line the corresponding mean ± SD. (For interpretation of the references to color in this figure legend, the reader is referred to the Web version of this article.)

– BDL: 2.03 ± 0.15 g/mL, SHAM: 2.23 ± 0.48 g/mL, cerebellum - BDL: 2.17 ± 0.34 g/mL, SHAM: 1.92 ± 0.53 g/mL). The difference in its macroscopic normalization factors (injected dose and weight) is not statistically significant between BDL and SHAM rats (Fig. 6C, weight - BDL: 328 ± 45 g, SHAM: 363± 31 g, dose – BDL: 70.51 ± 10.82 MBq, SHAM: 63.85 ± 12.77 MBq), leading to no difference in the SUV. However, the CMR_{glc} normalization factors (AIF curves and final glycemia) both display a difference between the groups, the latter being significant (BDL: 3.3 ± 1.5 mM, SHAM: 10.1 ± 2.1 mM, ****).

Interestingly, with the same injected dose of FDG in the tail vein for both groups, the average maximum value of the AIF curve from the BDL group is smaller than the one from the SHAM group. This observation suggests that the injected dose is not an accurate measure of the true tracer availability for the brain, since systemic effects, such as the metabolism of other organs, and particularly in this study, of the liver, might affect the blood FDG available for the brain. This physiological effect would have been overlooked using the SUV quantification. The same reasoning holds for the comparison between glycemia in the CMR_{glc} and the weight in the SUV. The latter is also a poor indicator of the physiology of the animal since BDL and SHAM rats have on average the same weight, but BDL rats have a much lower blood glycemia than the SHAM rats, which would have not been taken into account using the SUV.

Because the CMR_{glc} is derived from the kinetics of the 3-compartment model described in Fig. 1 and in equations (1) and (2), its expression involves local information on glucose uptake through the ratio between glycemia (C_p) and the total amount of tracer in the blood (the summed AIF) multiplied by the LC [21] (see equation (2)). However, the need for a carefully-sampled AIF is often the main difficulty preventing its wider use in metabolic imaging studies. In rodent studies, the small blood volume is a strong limitation for repeated manual sampling. Many technical challenges are also linked to the use of continuous measurements with external blood counters which often result in non-negligible physiological effects on the animal. Additionally, both manual blood sampling and external counters require the cannulation of veins or arteries, often rendering the experiment terminal. On the contrary, the proposed approach with the image-derived AIF provides a practical alternative to the manual blood sampling or external blood counters. It renders similar results [23] with particularly high temporal resolution, makes the measurement less invasive and allows for longitudinal studies with the same animal.

To further ensure a fair comparison between the groups, brain volumes were compared between BDL and SHAM rats and are presented in the supplementary material (Fig. S2). No overall brain atrophy was observed in BDL rats compared to SHAM rats (BDL brain volume – 1959.4 ± 41.0 mm^3, SHAM brain volume – 1939.2 ± 48.6 mm^3), ensuring that a given amount of tracer/plasma Glc is used by the same amount of brain tissue between the two groups.

Finally, the LC in the CMR_{glc} formula, in conjunction with the glycemia, also mirrors an important physiological aspect as it accounts for the competition between glucose and FDG and their respective affinity for blood brain barrier transporters and hexokinase. In particular in the present study, the glycemia values strongly differ between the BDL and SHAM groups. All kinetic constants from the 3-compartment model, both for the enzyme-mediated transport through the BBB and the enzyme-mediated phosphorylation for both substrates are described by a Michaelis-Menten equation modified to account for competitive substrates and mutual inhibition [53]. This competition is formally contained in the Lumped Constant expression from *Sokoloff* et al. [21]:

$$LC = \frac{1}{\Phi} \times \frac{k_1^*/(k_2^* + k_3^*)}{k_1/(k_2 + k_3)} \times \frac{V_m^*/K_m^*}{V_m/K_m} \tag{3}$$

where Φ is the fraction of G6P that will be further metabolized in glycolysis; the second fraction describing the ratio of kinetic constants of the radiotracer over the ones of natural Glc; and the last part of the fraction describes the ratio between Michaelis-Menten constants, $V_m^{(*)}$ the maximum velocity and $K_m^{(*)}$ Michaelis-Menten constants for the hexokinase reaction of either Glc or FDG. The LC constants were assumed identical for both groups. Importantly, the difference in blood glycemia and the resulting differential distribution of blood glucose versus FDG between groups would have been overlooked when

analyzing the glucose uptake with the SUV approach, for which we observed no significant difference in animal weights between the two groups.

For all the reasons mentioned above, when practically feasible, we suggest using a quantitative approach for the analysis of FDG uptake which enables the determination of the CMR_{glc} in studies involving group comparison where the physiology of the animal could greatly vary.

5. Conclusions

We report the first multimodal ^{18}F-FDG PET and localized ^{1}H MRS *in vivo* study in the type C HE BDL rat model. In addition, a refined FDG-PET analysis was developed to determine a quantitative and regional measurement of the cerebral metabolic rate of glucose in terms of 3D CMR_{glc} maps, based on an image-derived AIF. It revealed a 2-fold lower glucose uptake in the hippocampus and cerebellum of BDL versus SHAM rats. A concomitant increase in glutamine, a decrease in glutamate and in the osmolytes was measured with localized ^{1}H MRS in the same brain regions. This novel finding reopens the debate of energy failure in the pathophysiology of type C HE.

Acknowledgements

Supported by the SNSF project No 310030 173222 and the European Union's Horizon 2020 research and innovation program under the Marie Sklodowska-Curie grant agreement No 813120 (INSPiRE-MED). The authors would like to thank Dr. Corina Berset (CIBM) for her work in pilot PET experiments and the veterinary team at CIBM for support during experiments. This work was made possible thanks to the CIBM Center for Biomedical Imaging, a Swiss research center of excellence founded and supported by Lausanne University Hospital (CHUV), University of Lausanne (UNIL), Ecole Polytechnique Fédérale de Lausanne (EPFL), University of Geneva (UNIGE) and Geneva University Hospitals (HUG).

Appendix A. Supplementary data

Supplementary data to this article can be found online at https://doi.org/10.1016/j.ab.2022.114606.

References

[1] J. Bustamante, A. Rimola, P.J. Ventura, et al., Prognostic significance of hepatic encephalopathy in patients with cirrhosis, J. Hepatol. 30 (5) (1999) 890–895, https://doi.org/10.1016/s0168-8278(99)80144-5.
[2] M.D. Norenberg, Distribution of glutamine synthetase in the rat central nervous system, J. Histochem. Cytochem. Off. J. Histochem. Soc. 27 (3) (1979) 756–762, https://doi.org/10.1177/27.3.39099.
[3] C. Cudalbu, S.D. Taylor-Robinson, Brain edema in chronic hepatic encephalopathy, J. Clin. Exp. Hepatol. 9 (3) (2019) 362–382, https://doi.org/10.1016/j.jceh.2019.02.003.
[4] C. Bémeur, C. Cudalbu, G. Dam, A.S. Thrane, A.J.L. Cooper, C.F. Rose, Brain edema: a valid endpoint for measuring hepatic encephalopathy? Metab. Brain Dis. 31 (6) (2016) 1249–1258, https://doi.org/10.1007/s11011-016-9843-9.
[5] O. Braissant, V. Rackayová, K. Pierzchala, J. Grosse, V.A. McLin, C. Cudalbu, Longitudinal neurometabolic changes in the hippocampus of a rat model of chronic hepatic encephalopathy, J. Hepatol. 71 (3) (2019) 505–515, https://doi.org/10.1016/j.jhep.2019.05.022.
[6] K.V. Rama Rao, M.D. Norenberg, Brain energy metabolism and mitochondrial dysfunction in acute and chronic hepatic encephalopathy, Neurochem. Int. 60 (7) (2012) 697–706, https://doi.org/10.1016/j.neuint.2011.09.007.
[7] S. DeMorrow, C. Cudalbu, N. Davies, A.R. Jayakumar, C.F. Rose, ISHEN guidelines on animal models of hepatic encephalopathy, Liver. Int. Off. J. Int. Assoc. Study Liver 41 (7) (2021) 1474–1488, https://doi.org/10.1111/liv.14911.
[8] V. Rackayova, O. Braissant, V.A. McLin, C. Berset, B. Lanz, C. Cudalbu, 1H and 31P magnetic resonance spectroscopy in a rat model of chronic hepatic encephalopathy: in vivo longitudinal measurements of brain energy metabolism, Metab. Brain Dis. 31 (6) (2016) 1303–1314, https://doi.org/10.1007/s11011-015-9715-8.
[9] B. Lanz, V. Rackayova, O. Braissant, C. Cudalbu, MRS studies of neuroenergetics and glutamate/glutamine exchange in rats: extensions to hyperammonemic models, Anal. Biochem. 529 (2017) 245–269, https://doi.org/10.1016/j.ab.2016.11.021.
[10] C.R. Bosoi, C. Zwingmann, H. Marin, et al., Increased brain lactate is central to the development of brain edema in rats with chronic liver disease, J. Hepatol. 60 (3) (2014) 554–560, https://doi.org/10.1016/j.jhep.2013.10.011.
[11] B. Lanz, C. Cudalbu, V. McLin, M. Lepore, O. Braissant, R. Gruetter, In vivo 13C MRS investigation of alterations in cerebral oxidative metabolism in a chronic liver disease rat model, Proc. Intl. Soc. Mag. Reson. Med. 21 (2013) 1975.
[12] N.F. Cruz, T.E. Duffy, Local cerebral glucose metabolism in rats with chronic portacaval shunts, J. Cerebr. Blood Flow Metabol. 3 (3) (1983) 311–320, https://doi.org/10.1038/jcbfm.1983.46.
[13] J. Jessy, M.R. DeJoseph, R.A. Hawkins, Hyperammonaemia depresses glucose consumption throughout the brain, Biochem. J. 277 (Pt 3) (1991) 693–696, https://doi.org/10.1042/bj2770693.
[14] A.H. Lockwood, B.W. Murphy, K.Z. Donnelly, T.C. Mahl, S. Perini, Positron-emission tomographic localization of abnormalities of brain metabolism in patients with minimal hepatic encephalopathy, Hepatol. Baltim. Md. 18 (5) (1993) 1061–1068.
[15] A.H. Lockwood, K. Weissenborn, M. Bokemeyer, U. Tietge, W. Burchert, Correlations between cerebral glucose metabolism and neuropsychological test performance in nonalcoholic cirrhotics, Metab. Brain Dis. 17 (1) (2002) 29–40, https://doi.org/10.1023/A:1014000313824.
[16] W. Zhang, N. Ning, X. Li, et al., Impaired brain glucose metabolism in cirrhosis without overt hepatic encephalopathy: a retrospective 18F-FDG PET/CT study, Neuroreport 30 (11) (2019) 776–782, https://doi.org/10.1097/WNR.0000000000001284.
[17] R.F. Butterworth, Pathogenesis of hepatic encephalopathy: new insights from neuroimaging and molecular studies, J. Hepatol. 39 (2) (2003) 278–285, https://doi.org/10.1016/S0168-8278(03)00267-8.
[18] K. Vankadari, B.R. Mittal, R. Kumar, H. Singh, A. Bhattacharya, R.K. Dhiman, Detection of hepatic encephalopathy on 18F-FDG PET/CT brain images in a patient with decompensated liver cirrhosis, Clin. Nucl. Med. 43 (12) (2018) e486, https://doi.org/10.1097/RLU.0000000000002327.
[19] B. Hermann, M. Rudler, D. Galanaud, D. Thabut, N. Weiss, Magnetic resonance spectroscopy: a surrogate marker of hepatic encephalopathy? J. Hepatol. 71 (5) (2019) 1055–1057, https://doi.org/10.1016/j.jhep.2019.07.008.
[20] V.A. McLin, O. Braissant, C. Cudalbu, Reply to: "Magnetic resonance spectroscopy: a surrogate marker of hepatic encephalopathy?", J. Hepatol. 71 (5) (2019) 1057, https://doi.org/10.1016/j.jhep.2019.08.003.
[21] L. Sokoloff, M. Reivich, C. Kennedy, et al., The [14c]deoxyglucose method for the measurement of local cerebral glucose utilization: theory, procedure, and normal values in the conscious and anesthetized albino rat, J. Neurochem. 28 (5) (1977) 897–916, https://doi.org/10.1111/j.1471-4159.1977.tb10649.x.
[22] V. Berti, E. Vanzi, C. Polito, A. Pupi, Back to the future: the absolute quantification of cerebral metabolic rate of glucose, Clin. Transl. Imaging 1 (4) (2013) 289–296, https://doi.org/10.1007/s40336-013-0030-2.
[23] B. Lanz, C. Poitry-Yamate, R. Gruetter, Image-derived input function from the vena cava for 18F-FDG PET studies in rats and mice, J. Nucl. Med. Off. Publ. Soc. Nucl. Med. 55 (8) (2014) 1380–1388, https://doi.org/10.2967/jnumed.113.127381.
[24] M. Manto, J.M. Bower, A.B. Conforto, et al., Consensus paper: roles of the cerebellum in motor control—the diversity of ideas on cerebellar involvement in movement, Cerebellum 11 (2) (2012) 457–487, https://doi.org/10.1007/s12311-011-0331-9.
[25] F. Bahceci, B. Yildirim, M. Karincaoglu, I. Dogan, B. Sipahi, Memory impairment in patients with cirrhosis, J. Natl. Med. Assoc. 97 (2) (2005) 213–216.
[26] V. Mlynárik, G. Gambarota, H. Frenkel, R. Gruetter, Localized short-echo-time proton MR spectroscopy with full signal-intensity acquisition, Magn. Reson. Med. 56 (5) (2006) 965–970, https://doi.org/10.1002/mrm.21043.
[27] I. Tkác, Z. Starcuk, I.Y. Choi, R. Gruetter, In vivo 1H NMR spectroscopy of rat brain at 1 ms echo time, Magn. Reson. Med. 41 (4) (1999) 649–656, https://doi.org/10.1002/(sici)1522-2594(199904)41:4<649::aid-mrm2>3.0.co;2-g.
[28] R. Gruetter, Automatic, localized in vivo adjustment of all first- and second-order shim coils, Magn. Reson. Med. 29 (6) (1993) 804–811, https://doi.org/10.1002/mrm.1910290613.
[29] S.W. Provencher, Automatic quantitation of localized in vivo 1H spectra with LCModel, NMR Biomed. 14 (4) (2001) 260–264, https://doi.org/10.1002/nbm.698.
[30] C. Cudalbu, V. Mlynárik, R. Gruetter, Handling macromolecule signals in the quantification of the neurochemical profile, J. Alzheimers Dis. JAD. 31 (Suppl 3) (2012) S101–S115, https://doi.org/10.3233/JAD-2012-120100.
[31] C. Cudalbu, K.L. Behar, P.K. Bhattacharyya, et al., Contribution of macromolecules to brain 1 H MR spectra: experts' consensus recommendations, NMR Biomed. 34 (5) (2021), e4393, https://doi.org/10.1002/nbm.4393.
[32] V.V. Selivanov, Y. Picard, J. Cadorette, S. Rodrigue, R. Lecomte, Detector response models for statistical iterative image reconstruction in high resolution PET, Nucl. Sci. IEEE Trans. On 47 (2000) 1168–1175, https://doi.org/10.1109/23.856565.
[33] H.-M. Wu, G. Sui, C.-C. Lee, et al., In vivo quantitation of glucose metabolism in mice using small-animal PET and a microfluidic device, J. Nucl. Med. 48 (5) (2007) 837–845, https://doi.org/10.2967/jnumed.106.038182.
[34] R.W. Horton, B.S. Meldrum, H.S. Bachelard, ENZYMIC AND CEREBRAL METABOLIC EFFECTS OF 2-DEOXY-d-GLUCOSE, J. Neurochem. 21 (3) (1973) 507–520, https://doi.org/10.1111/j.1471-4159.1973.tb05996.x.
[35] A. Sols, R.K. Crane, Substrate specificity of brain hexokinase, J. Biol. Chem. 210 (2) (1954) 581–595.

[36] J. Tokugawa, L. Ravasi, T. Nakayama, K.C. Schmidt, L. Sokoloff, Operational lumped constant for FDG in normal adult male rats, J. Nucl. Med. 48 (1) (2007) 94–99.
[37] R.P. Woods, S.R. Cherry, J.C. Mazziotta, Rapid automated algorithm for aligning and reslicing PET images, J. Comput. Assist. Tomogr. 16 (4) (1992) 620–633.
[38] E.A. Papp, T.B. Leergaard, E. Calabrese, G.A. Johnson, J.G. Bjaalie, Waxholm space atlas of the sprague dawley rat brain, Neuroimage 97 (2014) 374–386, https://doi.org/10.1016/j.neuroimage.2014.04.001.
[39] B.B. Avants, N.J. Tustison, G. Song, P.A. Cook, A. Klein, J.C. Gee, A reproducible evaluation of ANTs similarity metric performance in brain image registration, Neuroimage 54 (3) (2011) 2033–2044, https://doi.org/10.1016/j.neuroimage.2010.09.025.
[40] T. Boehler, D. van Straaten, S. Wirtz, H.-O. Peitgen, A robust and extendible framework for medical image registration focused on rapid clinical application deployment, Comput. Biol. Med. 41 (6) (2011) 340–349, https://doi.org/10.1016/j.compbiomed.2011.03.011.
[41] J.H. Bothwell, C. Rae, R.M. Dixon, P. Styles, K.K. Bhakoo, Hypo-osmotic swelling-activated release of organic osmolytes in brain slices: implications for brain oedema in vivo, J. Neurochem. 77 (6) (2001) 1632–1640, https://doi.org/10.1046/j.1471-4159.2001.00403.x.
[42] H. Pasantes-Morales, A. Schousboe, Role of taurine in osmoregulation in brain cells: mechanisms and functional implications, Amino Acids 12 (3) (1997) 281–292, https://doi.org/10.1007/BF01373008.
[43] E. Flatt, O. Braissant, S. Mitrea, et al., 37 probiotics combined with rifaximin for the treatment of chronic hepatic encephalopathy: a longitudinal in vivo 1H-MRS study of brain metabolism using BDL rats, Off. J. Am. Coll. Gastroenterol. ACG 114 (2019) S19, https://doi.org/10.14309/01.ajg.0000582124.67482.93.
[44] P. Ott, H. Vilstrup, Cerebral effects of ammonia in liver disease: current hypotheses, Metab. Brain Dis. 29 (4) (2014) 901–911, https://doi.org/10.1007/s11011-014-9494-7.
[45] O. Cauli, M.T. Mansouri, A. Agusti, V. Felipo, Hyperammonemia increases GABAergic tone in the cerebellum but decreases it in the rat cortex, Gastroenterology 136 (4) (2009) 1359–1367, https://doi.org/10.1053/j.gastro.2008.12.057, e1-2.
[46] V. Felipo, Hepatic encephalopathy: effects of liver failure on brain function, Nat. Rev. Neurosci. 14 (12) (2013) 851–858, https://doi.org/10.1038/nrn3587.
[47] D. Simicic, K. Pierzchala, V. Rackaova, et al., 33 in vivo longitudinal 1H MRS study of hippocampal, cereberal and striatal metabolic changes in the adult brain using an animal model of chronic hepatic encephalopathy, Am. J. Gastroenterol. 114 (2019) S17, https://doi.org/10.14309/01.ajg.0000582108.29364.13.
[48] C.R. Bosoi, C.F. Rose, Oxidative stress: a systemic factor implicated in the pathogenesis of hepatic encephalopathy, Metab. Brain Dis. 28 (2) (2013) 175–178, https://doi.org/10.1007/s11011-012-9351-5.
[49] K. Pierzchala, D. Simicic, V. Rackaova, et al., 68 brain regional susceptibility to oxidative stress in a rat model of chronic hepatic encephalopathy, Am. J. Gastroenterol. 114 (2019) S33–S36, https://doi.org/10.14309/01.ajg.0000582248.03815.eb.
[50] R. Gruetter, E.J. Novotny, S.D. Boulware, D.L. Rothman, R.G. Shulman, 1H NMR studies of glucose transport in the human brain, J. Cerebr. Blood Flow Metabol. 16 (3) (1996) 427–438, https://doi.org/10.1097/00004647-199605000-00009.
[51] R. Gruetter, K. Ugurbil, E.R. Seaquist, Steady-state cerebral glucose concentrations and transport in the human brain, J. Neurochem. 70 (1) (1998) 397–408, https://doi.org/10.1046/j.1471-4159.1998.70010397.x.
[52] L. Baker, B. Lanz, F. Andreola, et al., New technologies – new insights into the pathogenesis of hepatic encephalopathy, Metab. Brain Dis. 31 (2016), https://doi.org/10.1007/s11011-016-9906-y.
[53] M. Dixon, E.C. Webb, Enzymes, second ed., Academic Press, 1964. https://www.elsevier.com/books/enzymes/dixon/978-1-4832-0057-6. (Accessed 21 June 2021).